



Technical Note

Extraction of Water Body Information from Remote Sensing Imagery While Considering Greenness and Wetness Based on Tasseled Cap Transformation

Chao Chen ¹, Huixin Chen ¹, Jintao Liang ¹, Wenlang Huang ^{2,*}, Wenxue Xu ³, Bin Li ⁴ and Jianqiang Wang ⁵

¹ Marine Science and Technology College, Zhejiang Ocean University, Zhoushan 316022, China; chenchao@zjou.edu.cn (C.C.); s20070700014@zjou.edu.cn (H.C.); liangjintao@zjou.edu.cn (J.L.)

² Physical and Military Training Education Department, Zhejiang Ocean University, Zhoushan 316022, China

³ Center for Marine Surveying and Mapping Research, First Institute of Oceanography, Ministry of Natural Resources, Qingdao 266061, China; xuwx@fio.org.cn

⁴ Beijing Vminfull Limited, Beijing 100086, China; li.bin@pku.edu.cn

⁵ Zhejiang Institute of Hydrogeology and Engineering Geology, Ningbo 315012, China; jason@bolts-nut.com

* Correspondence: 010015@zjou.edu.cn

Abstract: Water, as an important part of ecosystems, is also an important topic in the field of remote sensing. Shadows and dense vegetation negatively affect most traditional methods used to extract water body information from remotely sensed images. As a result, extracting water body information with high precision from a wide range of remote sensing images which contain complex ground-based objects has proved difficult. In the present study, a method used for extracting water body information from remote sensing imagery considers the greenness and wetness of ground-based objects. Ground objects with varied water content and vegetation coverage have different characteristics in their greenness and wetness components obtained by the Tasseled Cap transformation (TCT). Multispectral information can be output as brightness, greenness, and wetness by Tasseled Cap transformation, which is widely used in satellite remote sensing images. Hence, a model used to extract water body information was constructed to weaken the influence of shadows and dense vegetation. Jiangsu and Anhui provinces are located along the Yangtze River, China, and were selected as the research area. The experiment used the wide-field-of-view (WFOV) sensor onboard the Gaofen-1 satellite to acquire remotely sensed photos. The results showed that the contours and spatial extent of the water bodies extracted by the proposed method are highly consistent, and the influence of shadow and buildings is minimized; the method has a high Kappa coefficient (0.89), overall accuracy (92.72%), and user accuracy (88.04%). Thus, the method is useful in updating a geographical database of water bodies and in water resource management.



Citation: Chen, C.; Chen, H.; Liang, J.; Huang, W.; Xu, W.; Li, B.; Wang, J. Extraction of Water Body Information from Remote Sensing Imagery While Considering Greenness and Wetness Based on Tasseled Cap Transformation. *Remote Sens.* **2022**, *14*, 3001. <https://doi.org/10.3390/rs14133001>

Academic Editors: Qiusheng Wu, Xinyi Shen, Jun Li and Chengye Zhang

Received: 7 March 2022

Accepted: 19 June 2022

Published: 23 June 2022

Publisher's Note: MDPI stays neutral with regard to jurisdictional claims in published maps and institutional affiliations.



Copyright: © 2022 by the authors. Licensee MDPI, Basel, Switzerland. This article is an open access article distributed under the terms and conditions of the Creative Commons Attribution (CC BY) license (<https://creativecommons.org/licenses/by/4.0/>).

Keywords: remote sensing imagery; water body extraction; Tasseled Cap transformation; WFOV onboard Gaofen-1; accuracy evaluation

1. Introduction

Water is an important resource for human survival and economic development [1–4]. Whether water is treated as an environmental factor, as a resource, or as a cause of flood disasters, the monitoring and investigation of the nature of water bodies have great significance in the use of natural resources; it is also important in land use planning, development and protection of the environment, and in flood protection and mitigation [5–7]. Remote sensing satellite observations can effectively overcome all kinds of the limitations that may be encountered in ground mapping, with the graphics of the landscape recorded numerically and processed by the computers [8–10]. Remote sensing satellite images cover the entire Earth with high resolution, repeatable observation, and multispectral images, which can accurately record rivers, lakes, coastlines, tidal conditions, as well as related

ground information and allow researchers to determine the range of a water body quickly and accurately; the cost of land-based surveys are saved while remotely sensed images provide many economic and social benefits [11–14].

Since the 1970s, researchers have conducted a considerable amount of research on the extraction of boundaries between water bodies and other ground-based objects [15–18]. From the earliest efforts in edge detection and threshold segmentation to the application of deep learning, the methods for extracting water body information have been developing over time with continuous progress [19–21]. The methods used to extract water body information from remote sensing imagery can be divided into three categories: (i) the single band threshold-based method, (ii) the spectrum photometric-based method, and (iii) the water body index-based method [22–25]. (i) The single band threshold-based method is an early commonly used method that uses a single band of a remote sensing image, the reflectivity of water is significantly lower or higher than other features, and a water body can be automatically extracted by setting the threshold [26–28]. The process of extracting water bodies using the single band threshold-based method is relatively simple, and the effects of extracting local water body information are clearly visible; nevertheless, dense vegetation, mountain shadows, and the water body spectrum cannot always be correctly distinguished while small water bodies cannot be extracted using this method [29–31]. (ii) The spectrum photometric-based method extracts water bodies by searching for the difference between the characteristics of the spectral curve of a water body and other features; this method can extract water bodies as well as distinguish water bodies from shadows, making it suitable for the extraction of water bodies in mountain plateaus [32–35]. For plains, this method can extract the wider part of lakes, larger rivers, and smaller rivers, but a phenomenon known as staggered buildings can create problems; however, a threshold can be used to judge the conditions for the extraction of water bodies from small rivers and those of larger urban areas [36–38]. In addition to buildings, this method is also affected by clouds. (iii) The water body index-based method is performed by using normalized difference processing of specific wavelengths of ground-based objects to highlight water body information in remote sensing images [39–42]. The method is very precise, has wide applicability, is simple to operate, and is currently the most widely used and developed method [43–45]. This method can effectively eliminate shadow pixels and improve the accuracy of shadow extraction or of other dark surface areas; however, the reflective surfaces of urban areas, such as ice, snow, and reflective roofs, may be accidentally classified as water.

Tasseled Cap transformation (TCT) is a special type of principal component transformation, which combines complex factors into several components while introducing multi-faceted variables, and it simplifies the problem and, at the same time, obtains more scientifically sound and effective data information [46]. In this paper, we aim to provide a detailed guide on how to develop an approach capable of providing estimates of water body information from the wide-field-of-view (WFV) image of the Gaofen-1 satellite with a wide range. This approach both considers the greenness and wetness of ground-based objects obtained by TCT to weaken the influence of shadows and dense vegetation. This paper is of great significance for updating basic geographic information and water resources investigation.

2. Materials and Methods

2.1. Study Area

The study area is located at the intersection of Jiangsu and Anhui provinces, China, which is a part of the Yangtze River Delta. The Yangtze River forms the Yangtze River Delta, an alluvial plain, before entering the sea [47–49]. The delta covers parts of two provinces, Zhejiang and Jiangsu, and the city of Shanghai [50,51]. This densely populated low-lying plain also supports a well-developed area of agriculture; the plain is covered by a dense river network, agricultural areas, and more than 200 lakes. The research area includes a variety of terrain such as plains, lakes, and mountains with numerous urban areas (Figure 1).

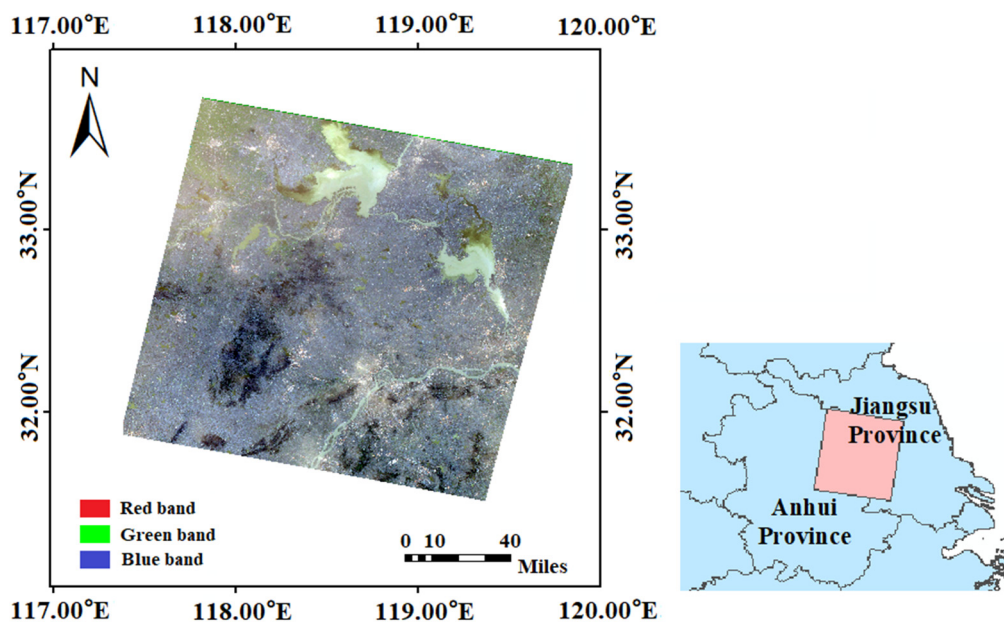


Figure 1. Remotely sensed photo of the study area. An inset map shows the location of the study area within the Anhui and Jiangsu provinces.

2.2. Data

In the study, the image of the covered study area was acquired on 31 December 2016 by the WFV camera onboard the Gaofen-1 satellite. Gaofen-1 (in the Chinese language, gao fen means high resolution) is the first of a series of high-resolution optical Earth observation satellites of the China National Space Administration, Beijing, China, which is configured with two 2 m panchromatic/8 m resolution multispectral cameras and a set of four 16 m resolution multispectral medium-resolution wide-field cameras [52]. The WFV sensor with 16 m spatial resolution consists of three visible light bands (0.45–0.52 μm , 0.52–0.59 μm , 0.63–0.69 μm) and a near-infrared band (0.77–0.89 μm) [53–55]. With the satellite's four-day repetition cycle, the combination of high temporal and spatial resolution is achieved; this combination has played an important role in land and resources investigation and in the dynamic monitoring of the environment and climate change as well as in supporting precision agriculture and urban planning [56–58].

For the Gaofen-1 satellite data, no definite coefficient for TCT has yet to be developed; however, by comparing the parameters of the WFV cameras sensor of Gaofen-1 with known satellite sensors with Tasseled Cap transform coefficients, it was found that the WFV sensor and the IKONOS satellite sensor have a similar number of bands and spectral range of bands [59]. As the TCT conversion coefficient is fixed and determined by the band number and band range of a sensor, the conversion coefficient of the IKONOS satellite was selected in this paper (Table 1) [60,61].

It can be seen from Table 1 that (1) All band coefficients used to calculate the brightness component are positive, each band makes a positive contribution to the brightness component, and the contribution sequence is near-infrared band > red band > green band > blue band. (2) The near-infrared band has a positive contribution to the greenness component, while the other bands have a negative contribution, and the contribution sequence is near-infrared band > green band > red band > blue band. (3) The red band has a positive contribution to the wetness component, while the other bands have a negative contribution, and the contribution sequence is red band > blue band > green band > near-infrared band. (4) The green band has a positive contribution to the yellowness component, while the other bands have a negative contribution, and the contribution sequence is green band > blue band > red band > near-infrared band.

Table 1. The weights of the Tasseled Cap transformation for the WFV sensor onboard the Gaofen-1 satellite.

	Blue Band	Green Band	Red Band	Near-Infrared Band
Brightness component	0.326	0.509	0.560	0.567
Greenness component	−0.311	−0.356	−0.325	0.819
Wetness component	−0.612	−0.312	0.722	−0.081
Yellowness component	−0.650	0.719	−0.243	−0.031

2.3. Method

Tasseled Cap transformation (TCT), also known as Kauth–Thomas transformation, was first reported in 1976 by using maximum segment size data on the growth of crops and vegetation; it consisted of four bands in the maximum segment size analysis [62–64]. In the four-dimensional space, the spectral data points of vegetation are regularly distributed, forming a hat-like shape; therefore, this transformation is named a Tasseled Cap transformation [65,66]. TCT has been widely used in many fields, such as crop type recognition [67], crop growth monitoring [68], remote sensing ecological assessment [69,70], and monitoring of land surface changes [71,72]. It also has important application value in forest type classification [73], distinguishing forest density [74], and biomass inversion [75,76].

For satellite remote sensing imagery, a TCT can compress a multispectral image into a sum of a set of components, each of which corresponds to a weighted index [66]. The weighted index can reflect each pixel in the original multispectral image.

The TCT is as Equation (1) [62–64]:

$$y = cx + a \quad (1)$$

where y is the component in multispectral space after the transformation, x corresponds to the multispectral bands before the transformation, c is the transformation coefficient, which is related to the sensor onboard a satellite, and a is a constant used to avoid negative values.

In this new spectral space after the TCT occurs, the first four components (brightness, greenness, wetness, and yellowness components) are important. The brightness component reflects the comprehensive effect of total reflectivity; the greenness component is related to vegetation cover, leaf base cover index, and biomass; the wetness component reflects the moisture condition of the ground-based objects, and the yellowness component indicates the maturity of vegetation [49,77,78].

The size of the component index corresponding to each pixel can reflect the correlation between its corresponding features and these components (Figure 2). Since different features have different correlations with the four components, these pixels are based on the component values in a 4-dimensional space. The distribution forms different settlements. The pixels in each settlement correspond to the same kind of features, and the boundaries are obvious. It is easy to find the difference between different objects and extract the water information.

Tasseled Cap transformation uses principal component analysis, and its conversion coefficient is fixed, which is determined by the number of frequency bands and spectral range of frequency bands. Therefore, it is independent of individual images so that the soil brightness and greenness can be compared between different images. Compared with other ground-based objects, water bodies have unique characteristics in their greenness and wetness components. Therefore, based on the characteristics of the TCT, a method for extracting water body information from remote sensing imagery has been proposed for use in processing remote sensing imagery; water body information can be extracted accurately and the influence of shadows and dense vegetation can be weakened.

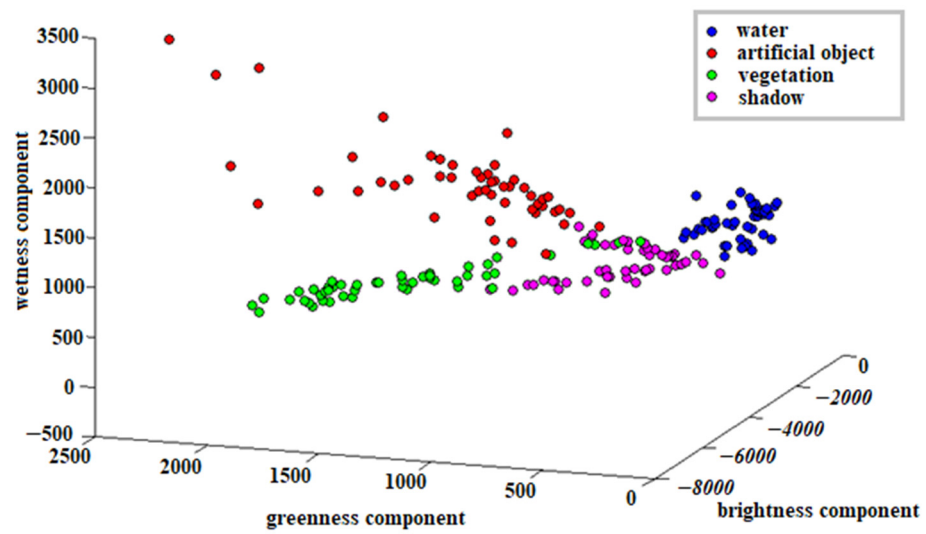


Figure 2. Scatter plot of ground-based objects in the space of TCT.

The variation in water content and vegetation coverage of the ground-based objects will cause water bodies to show unique characteristics in the feature space after TCT. The overall workflow of the method for extracting water body information from remote sensing imagery considering greenness and wetness can be divided into four steps: (a) pre-processing, (b) TCT, (c) extraction of water body information, and (d) accuracy assessment (Figure 3).

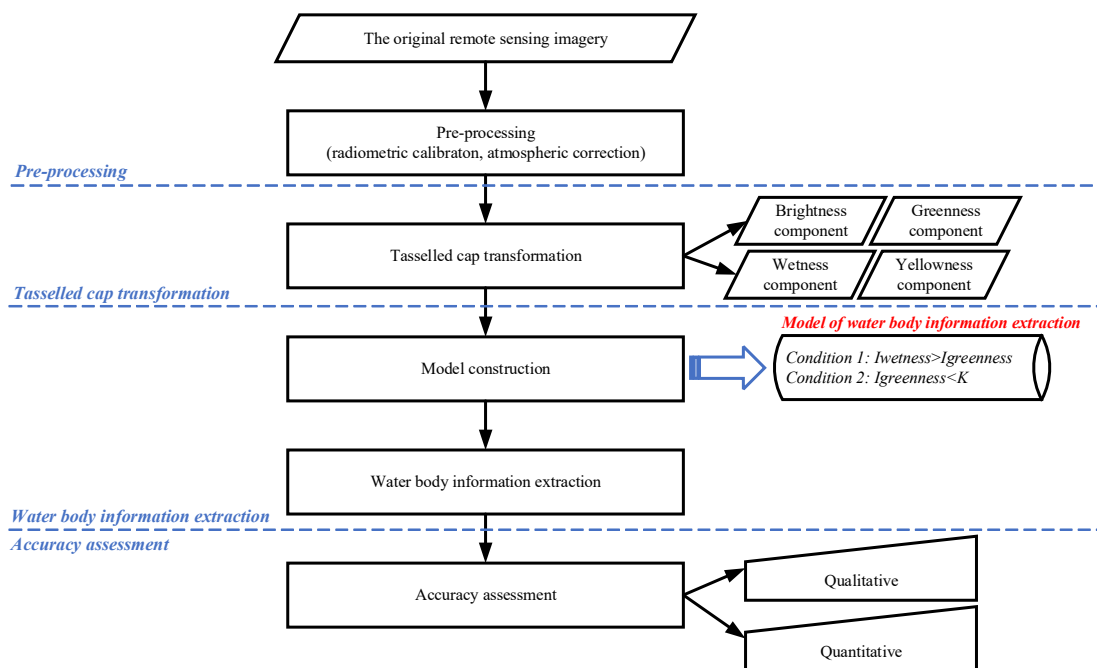


Figure 3. Flowchart of the proposed method.

First, the original remote sensing image data were pre-processed with radiometric calibration and atmospheric correction to eliminate the deviation caused by atmosphere absorption and scattering of light. Second, the correlated remote sensing image information was converted into uncorrelated linear information using TCT; four components were obtained: brightness, greenness, wetness, and yellowness. Third, based on the greenness and wetness components, the difference between the water body and other ground-based objects (vegetation, man-made object, shadow) was analyzed and the model was con-

structed to extract water body information. Finally, an accuracy assessment was carried out by calculating the Kappa Coefficient, overall accuracy, and user accuracy.

3. Results

3.1. Water Body Information Extraction from Remote Sensing Imagery While Considering Greenness and Wetness

The original remote sensing image was pre-processed with radiometric calibration and atmospheric correction to eliminate most of the deviation caused by the atmosphere, and Environment for Visualizing Images (ENVI) version 4.8 software has been used to perform statistical and visual analyzes on satellite imagery. Then, a TCT was performed to obtain the four components, brightness, greenness, wetness, and yellowness, using the weights in Table 1. The results are shown in Figure 4.

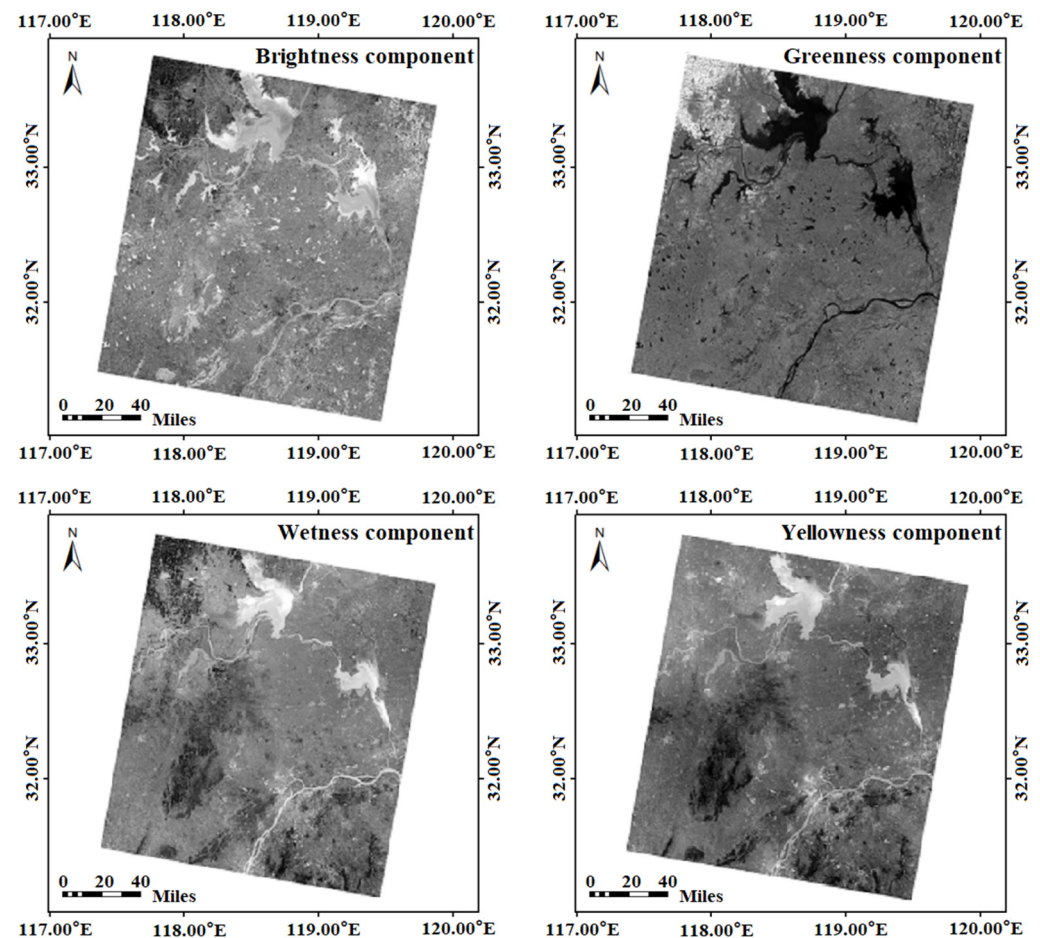


Figure 4. The TCT components of the WFV cameras onboard the Gaofen-1 satellite.

In the feature map (Figure 5), the water bodies show different distribution characteristics from those of vegetation (including dry field), man-made features (including roads, residential, and industrial land), and shadow (mainly mountain and building shadows).

As can be seen from Figures 4 and 5, the water bodies correspond to relatively high and low values in the wetness and greenness components, respectively; vegetation has a relatively high value in the greenness component; meanwhile, shadows and man-made objects have more diverse reflectivity due to the variety of their species. By adding an auxiliary line $I_{wetness} = I_{greenness}$ to Figure 5, it is easy to see that the corresponding pixels of water bodies are all located below the auxiliary line, and the vegetation and shadows are all located above the line; therefore, the condition of " $I_{wetness} > I_{greenness}$ " can easily be used to divide the water bodies from the shadows and vegetation. However, some man-made

objects still fall below the auxiliary line; one can see a clear gap exists between the greenness component of these man-made objects and the greenness component of the water body. Therefore, the thresholding condition “ $I_{greenness} < K$ ” was set to distinguish the water bodies from the man-made object.

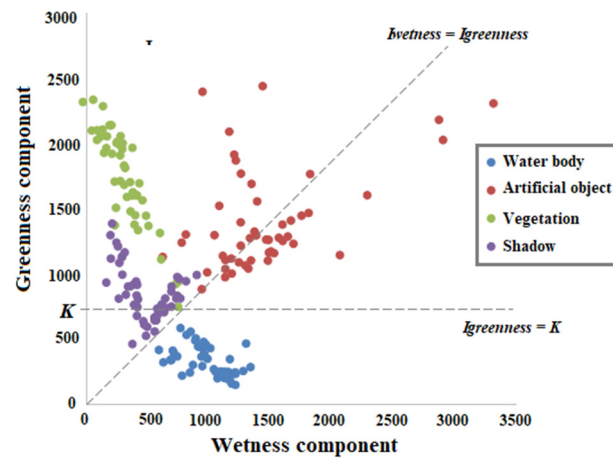


Figure 5. The distribution characteristics of ground-based objects in the feature map generated by Tassel Cap transformation components.

Equation (2) provides the formula for extracting water body information as follows:

$$\begin{cases} I_{wetness} > I_{greenness} \\ I_{greenness} < K \end{cases} \quad (2)$$

where $I_{wetness}$ and $I_{greenness}$ are the wetness and greenness components obtained by TCT, respectively, and K is the empirical constant of the greenness component, usually 750.

The greenness and wetness components obtained from the TCT were used to extract water body information with the support of Equation (1). The extraction results are shown in Figure 6.

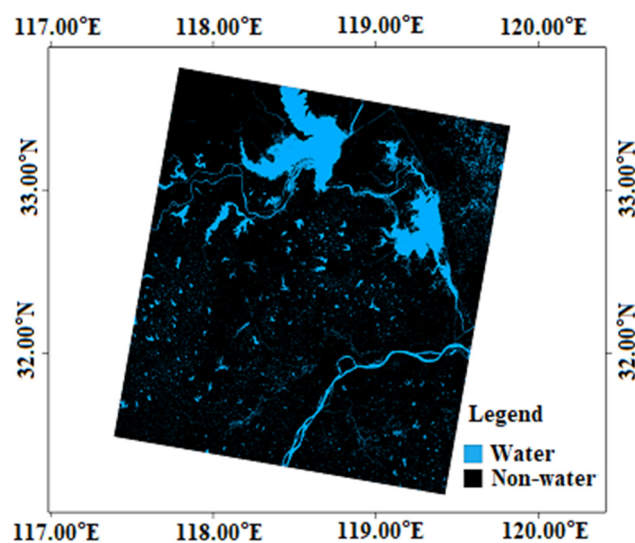


Figure 6. The water body information extracted using the proposed method and ENVI 4.8 software has been used to perform statistical and visual analyzes on satellite imagery.

By visually observing the difference between the extraction results and the original remote sensing image, Figures 1 and 6 show that the extracted water body information is

consistent with the visual results regardless of the size and contour of water bodies and can effectively remove the shadows of mountains, buildings, and clouds. However, man-made buildings cause some errors.

3.2. Accuracy Assessment

Accuracy assessment is an important part of information extraction from remote sensing imagery, and using the confusion matrix to calculate the Kappa coefficient, overall accuracy (OA), and user accuracy (UA) is a common method for accuracy assessment [79–81]. The real boundary of the water bodies was obtained by visual interpretation from the Gaofen-1 satellite image, and the Kappa coefficient, OA, and UA were calculated based on visual interpretation and the extracted results. The water bodies were obtained by the proposed method and the results were obtained by single band threshold-based method, spectrum photometric-based method, normalized difference water index-based method (NDWI-based method), water ratio index-based method (WRI-based method), and automated water extraction index-based method (AWEI_{sh}-based method) which were compared to perform a quantitative evaluation of the results [82–84], and the experiment was carried out by ENVI 4.8 software.

Table 2 shows that the Kappa coefficient, OA, and UA of the proposed method are all higher than those of the traditional methods. This indicates that the water body information extracted using the proposed method is consistent with the visual interpretation results, and the method considering the greenness and wetness of ground-based objects is reliable and accurate.

Table 2. Quantitative evaluation of extracting water body information.

Method	Formula	Kappa Coefficient	OA (%)	UA (%)
Single-band threshold-based method	$\rho_{NIR} < 0$	0.77	86.63	80.28
Spectrum photometric-based method	$\rho_{green} + \rho_{red} > 2 \times \rho_{NIR}$	0.86	90.05	83.51
NDWI-based method	$(\rho_{green} - \rho_{NIR}) / (\rho_{green} + \rho_{NIR}) > 0$	0.88	93.35	87.69
WRI-based method	$(\rho_{green} + \rho_{red}) / (2 \times \rho_{NIR}) > 1$	0.83	87.08	84.92
AWEI _{sh} -based method	$(\rho_{blue} + 2.5 \times \rho_{green} - 3.25 \times \rho_{NIR}) > 0$	0.78	80.34	78.59
The proposed method	$I_{wetness} > I_{greenness}$ and $I_{greenness} < 750$	0.91	97.02	90.81

Note: ρ is the reflectance of remote sensing imagery; *red*, *green*, *NIR* are red, green, and near-infrared bands, respectively; $I_{wetness}$ and $I_{greenness}$ are wetness and greenness obtained by TCT, respectively.

4. Discussion

The components obtained by the TCT are associated with water content and vegetation coverage of ground-based objects, which is helpful in extracting water body information quickly and simply by using remote sensing images in a wide range. Following remote sensing image pre-processing, TCT, and model construction considering greenness and wetness, the water body information can be extracted accurately. Unfortunately, there are some factors affecting the extraction accuracy of the water body information. First, a pixel in the remote sensing image measures the combined reflectance of all ground objects contained on the ground of the same size as the spatial resolution [4,28,49]. Therefore, mixed pixels cause boundaries between land and water body to become vague and affect the accurate statistics of the extracted water body information. Second, the threshold values in the constructed model are obtained by the statistics of the sampling points and are representative of the study area [3,10,49]. Therefore, the use of the model in other regions may produce uncertainty errors. Third, the water surface can be shaded by vegetation covering the bank zone, and then the surface morphology of extracted water body information is affected [85–87]. Therefore, considering the characteristics of smooth edges of banks, edge restoration of extracted water body information is also worth discussing.

5. Conclusions

The present study developed a method for extracting water body information from remote sensing imagery by considering the greenness and wetness of ground-based objects using TCT. This was applied to reduce the influence caused by shadows and dense vegetation to achieve simple, fast, and accurate extraction of water body information. The experiment using the WFV sensor onboard the Gaofen-1 satellite was carried out along the border between Jiangsu and Anhui of the Yangtze River Delta, China, to demonstrate and validate this method. Based on the qualitative and quantitative evaluations, the proposed method is accurate, and the validity and practicality of the proposed method have been verified.

The proposed method has high precision and is simple to operate. However, some weakness remained that has not been eliminated in this experiment. The influence of mixed pixels caused the boundaries of water body information extracted from remote sensing imagery to be inconsistent with the actual boundaries of water bodies in the real world. In addition, using the coefficient of IKONOS to perform the TCT of data collected by the WFV sensor onboard the Gaofen-1 satellite also leads to an uncertain effect in the extraction of water body information. Therefore, developing a mixed pixel decomposition method that can be used to extract the boundaries of water body information more accurately will need to be a follow-up research study. Obtaining the coefficient of the WFV imagery acquired using the Gaofen-1 satellite to reduce the uncertain influence of water body information extraction is another direction that will need continuing efforts.

Author Contributions: Conceptualization, C.C. and W.H.; methodology, C.C. and W.X.; software, C.C., H.C., J.L. and W.H.; validation, C.C., H.C., J.L. and B.L.; formal analysis, C.C., H.C. and J.L.; investigation, C.C. and J.W.; resources, H.C. and J.L.; data curation, C.C.; writing—original draft preparation, C.C., H.C. and J.L.; writing—review and editing, C.C., H.C., W.H., W.X., B.L. and J.W.; project administration, C.C.; funding acquisition, C.C., W.H., B.L. and J.W. All authors have read and agreed to the published version of the manuscript.

Funding: This study was funded by the National Key R&D Program of China (Grant Number: 2021YFB3901305), in part by the National Natural Science Foundation of China (Grant Number: 42171311), in part by the Fundamental Research Funds for Zhejiang Provincial Universities and Research Institutes (Grant Numbers: 2021R005, 2021JZ001), in part by the Project of Beijing VMinFull Limited (Grant Number: VMF2021RS), in part by the Training Program of Excellent Master Thesis of Zhejiang Ocean University.

Data Availability Statement: The satellite remote sensing images of Gaofen-1 were provided by the Chinese Academy of Science (www.ids.ceode.ac.cn). All Gaofen-1 data used in the study is not applicable.

Acknowledgments: The authors would like to thank the editors and the anonymous reviewers for their outstanding comments and suggestions, which greatly helped them to improve the technical quality and presentation of this manuscript.

Conflicts of Interest: The authors declare no conflict of interest.

References

1. Jain, S.K.; Saraf, A.K.; Goswami, A.; Ahmad, T. Flood inundation mapping using NOAA AVHRR data. *Water Resour. Manag.* **2006**, *20*, 949–959. [[CrossRef](#)]
2. Duan, Z.; Bastiaanssen, W. Estimating water volume variations in lakes and reservoirs from four operational satellite altimetry databases and satellite imagery data. *Remote Sens. Environ.* **2013**, *134*, 403–416. [[CrossRef](#)]
3. Sun, W.; Peng, J.; Yang, G.; Du, Q. Correntropy-Based Sparse Spectral Clustering for Hyperspectral Band Selection. *IEEE Geosci. Remote Sens. Lett.* **2020**, *17*, 484–488. [[CrossRef](#)]
4. Wang, L.; Chen, C.; Xie, F.; Hu, Z.; Zhang, Z.; Chen, H.; He, X.; Chu, Y. Estimation of the value of regional ecosystem services of an archipelago using satellite remote sensing technology: A case study of Zhoushan Archipelago, China. *Int. J. Appl. Earth Obs. Geoinf.* **2021**, *105*, 102616. [[CrossRef](#)]
5. Sethre, P.R.; Rundquist, B.C.; Todhunter, P.E. Remote Detection of Prairie Pothole Ponds in the Devils Lake Basin, North Dakota. *GIScience Remote Sens.* **2005**, *42*, 277–296. [[CrossRef](#)]

6. Masocha, M.; Dube, T.; Makore, M.; Shekede, M.D.; Funani, J. Surface water bodies mapping in Zimbabwe using Landsat 8 OLI multispectral imagery: A comparison of multiple water indices. *Phys. Chem. Earth Parts A/B/C* **2018**, *106*, 63–67. [[CrossRef](#)]
7. Pôças, I.; Calera, A.; Campos, I.; Cunha, M. Remote sensing for estimating and mapping single and basal crop coefficients: A review on spectral vegetation indices approaches. *Agric. Water Manag.* **2020**, *233*, 106081. [[CrossRef](#)]
8. Chen, H.; Chen, C.; Zhang, Z.; Lu, C.; Wang, L.; He, X.; Chu, Y.; Chen, J. Changes of the spatial and temporal characteristics of land-use landscape patterns using multi-temporal Landsat satellite data: A case study of Zhoushan Island, China. *Ocean Coast. Manag.* **2021**, *213*, 105842. [[CrossRef](#)]
9. Fu, J.; Chen, C.; Chu, Y. Spatial-temporal variations of oceanographic parameters in the Zhoushan sea area of the East China Sea based on remote sensing datasets. *Reg. Stud. Mar. Sci.* **2019**, *28*, 100626. [[CrossRef](#)]
10. Chen, C.; Wang, L.; Zhang, Z.; Lu, C.; Chen, H.; Chen, J. Construction and application of quality evaluation index system for remote-sensing image fusion. *J. Appl. Remote Sens.* **2021**, *16*, 012006. [[CrossRef](#)]
11. Han, C.; Zhang, B.; Chen, H.; Wei, Z.; Liu, Y. Spatially distributed crop model based on remote sensing. *Agric. Water Manag.* **2019**, *218*, 165–173. [[CrossRef](#)]
12. Ranjan, S.; Sarvaiya, J.N.; Patel, J.N. Integrating Spectral and Spatial features for Hyperspectral Image Classification with a Modified Composite Kernel Framework. *PFG—J. Photogramm. Remote Sens. Geoinf. Sci.* **2019**, *87*, 275–296. [[CrossRef](#)]
13. Chen, Y.; Ming, D.; Lv, X. Superpixel based land cover classification of VHR satellite image combining multi-scale CNN and scale parameter estimation. *Earth Sci. Inform.* **2019**, *12*, 341–363. [[CrossRef](#)]
14. Sun, W.; Yang, G.; Peng, J.; Du, Q. Lateral-Slice Sparse Tensor Robust Principal Component Analysis for Hyperspectral Image Classification. *IEEE Geosci. Remote Sens. Lett.* **2020**, *17*, 107–111. [[CrossRef](#)]
15. Gautam, V.K.; Gaurav, P.K.; Murugan, P.; Annadurai, M. Assessment of Surface Water Dynamics in Bangalore Using WRI, NDWI, MNDWI, Supervised Classification and K-T Transformation. *Aquat. Procedia* **2015**, *4*, 739–746. [[CrossRef](#)]
16. Huang, X.; Xie, C.; Fang, X.; Zhang, L. Combining Pixel- and Object-Based Machine Learning for Identification of Water-Body Types from Urban High-Resolution Remote-Sensing Imagery. *IEEE J. Sel. Top. Appl. Earth Obs. Remote Sens.* **2015**, *8*, 2097–2110. [[CrossRef](#)]
17. He, X.; Chen, C.; Liu, Y.; Chu, Y. Inundation Analysis Method for Urban Mountainous Areas Based on Soil Conservation Service Curve Number (SCS-CN) Model Using Remote Sensing Data. *Sensors Mater.* **2020**, *32*, 3813. [[CrossRef](#)]
18. Valderrama-Landeros, L.; Flores-de-Santiago, F. Assessing coastal erosion and accretion trends along two contrasting subtropical rivers based on remote sensing data. *Ocean. Coast. Manag.* **2019**, *169*, 58–67. [[CrossRef](#)]
19. Teodoro, A.C.; Goncalves, H.; Veloso-Gomes, F.; Goncalves, J.A. Modeling of the Douro River Plume Size, Obtained Through Image Segmentation of MERIS Data. *IEEE Geosci. Remote Sens. Lett.* **2009**, *6*, 87–91. [[CrossRef](#)]
20. Malahlela, O.E. Inland waterbody mapping: Towards improving discrimination and extraction of inland surface water features. *Int. J. Remote Sens.* **2016**, *37*, 4574–4589. [[CrossRef](#)]
21. Su, H.; Peng, Y.; Xu, C.; Feng, A.; Liu, T. Using improved DeepLabv3+ network integrated with normalized difference water index to extract water bodies in Sentinel-2A urban remote sensing images. *J. Appl. Remote Sens.* **2021**, *15*, 018504. [[CrossRef](#)]
22. Jawak, S.D.; Kulkarni, K.; Luis, A.J. A Review on Extraction of Lakes from Remotely Sensed Optical Satellite Data with a Special Focus on Cryospheric Lakes. *Adv. Remote Sens.* **2015**, *4*, 196–213. [[CrossRef](#)]
23. Fisher, A.; Flood, N.; Danaher, T. Comparing Landsat water index methods for automated water classification in eastern Australia. *Remote Sens. Environ.* **2016**, *175*, 167–182. [[CrossRef](#)]
24. Sarp, G.; Ozelcik, M. Water body extraction and change detection using time series: A case study of Lake Burdur, Turkey. *J. Taibah Univ. Sci.* **2017**, *11*, 381–391. [[CrossRef](#)]
25. Li, D.; Wu, B.; Chen, B.; Xue, Y.; Zhang, Y. Review of water body information extraction based on satellite remote sensing. *J. Tsinghua Univ. (Sci. Technol.)* **2020**, *60*, 147–161.
26. Lira, J. Segmentation and morphology of open water bodies from multispectral images. *Int. J. Remote Sens.* **2006**, *27*, 4015–4038. [[CrossRef](#)]
27. Grodsky, S.; Reverdin, G.; Carton, J.; Coles, V.J. Year-to-year salinity changes in the Amazon plume: Contrasting 2011 and 2012 Aquarius/SACD and SMOS satellite data. *Remote Sens. Environ.* **2014**, *140*, 14–22. [[CrossRef](#)]
28. Chen, C.; Fu, J.Q.; Sui, X.X.; Lu, X.; Tan, A.H. Construction and application of knowledge decision tree after a disaster for water body information extraction from remote sensing images. *J. Remote Sens.* **2018**, *22*, 792–801.
29. Wilson, E.H.; Sader, S.A. Detection of forest harvest type using multiple dates of Landsat TM imagery. *Remote Sens. Environ.* **2002**, *80*, 385–396. [[CrossRef](#)]
30. Sharma, D.; Singhai, J. An Object-Based Shadow Detection Method for Building Delineation in High-Resolution Satellite Images. *PFG—J. Photogramm. Remote Sens. Geoinf. Sci.* **2019**, *87*, 103–118. [[CrossRef](#)]
31. Vanama, V.S.K.; Mandal, D.; Rao, Y.S. GEE4FLOOD: Rapid mapping of flood areas using temporal Sentinel-1 SAR images with Google Earth Engine cloud platform. *J. Appl. Remote Sens.* **2020**, *14*, 034505. [[CrossRef](#)]
32. Rogers, A.S.; Kearney, M.S. Reducing signature variability in unmixing coastal marsh Thematic Mapper scenes using spectral indices. *Int. J. Remote Sens.* **2004**, *25*, 2317–2335. [[CrossRef](#)]
33. Jain, S.K.; Singh, R.D.; Jain, M.; Lohani, A.K. Delineation of Flood-Prone Areas Using Remote Sensing Techniques. *Water Resour. Manag.* **2005**, *19*, 333–347. [[CrossRef](#)]

34. Yang, Z.; Wang, L.; Sun, W.; Xu, W.; Tian, B.; Zhou, Y.; Yang, G.; Chen, C. A New Adaptive Remote Sensing Extraction Algorithm for Complex Muddy Coast Waterline. *Remote Sens.* **2022**, *14*, 861. [[CrossRef](#)]
35. Ahmed, A.; Drake, F.; Nawaz, R.; Woulds, C. Where is the coast? Monitoring coastal land dynamics in Bangladesh: An integrated management approach using GIS and remote sensing techniques. *Ocean. Coast. Manag.* **2018**, *151*, 10–24. [[CrossRef](#)]
36. Guttler, F.; Niculescu, S.; Gohin, F. Turbidity retrieval and monitoring of Danube Delta waters using multi-sensor optical remote sensing data: An integrated view from the delta plain lakes to the western–northwestern Black Sea coastal zone. *Remote Sens. Environ.* **2013**, *132*, 86–101. [[CrossRef](#)]
37. Wan, W.; Long, D.; Hong, Y.; Ma, Y.; Yuan, Y.; Xiao, P.; Duan, H.; Han, Z.; Gu, X. A lake data set for the Tibetan Plateau from the 1960s, 2005, and 2014. *Sci. Data* **2016**, *3*, 160039. [[CrossRef](#)]
38. Wei, B.; Li, Y.; Suo, A.; Zhang, Z.; Xu, Y.; Chen, Y. Spatial suitability evaluation of coastal zone, and zoning optimisation in Ningbo, China. *Ocean Coast. Manag.* **2021**, *204*, 105507. [[CrossRef](#)]
39. McFeeters, S.K. The use of the Normalized Difference Water Index (NDWI) in the delineation of open water features. *Int. J. Remote Sens.* **1996**, *17*, 1425–1432. [[CrossRef](#)]
40. Xu, H. Modification of normalised difference water index (NDWI) to enhance open water features in remotely sensed imagery. *Int. J. Remote Sens.* **2006**, *27*, 3025–3033. [[CrossRef](#)]
41. Feyisa, G.L.; Meilby, H.; Fensholt, R.; Proud, S.R. Automated Water Extraction Index: A new technique for surface water mapping using Landsat imagery. *Remote Sens. Environ.* **2014**, *140*, 23–35. [[CrossRef](#)]
42. Ahmed, N.; Howlader, N.; Hoque, M.A.-A.; Pradhan, B. Coastal erosion vulnerability assessment along the eastern coast of Bangladesh using geospatial techniques. *Ocean Coast. Manag.* **2021**, *199*, 105408. [[CrossRef](#)]
43. Zhang, G.; Yao, T.; Xie, H.; Zhang, K.; Zhu, F. Lakes' state and abundance across the Tibetan Plateau. *Chin. Sci. Bull.* **2014**, *59*, 3010–3021. [[CrossRef](#)]
44. Liao, H.-Y.; Wen, T.-H. Extracting urban water bodies from high-resolution radar images: Measuring the urban surface morphology to control for radar's double-bounce effect. *Int. J. Appl. Earth Obs. Geoinf.* **2020**, *85*, 102003. [[CrossRef](#)]
45. Xia, Z.; Guo, X.; Chen, R. Automatic extraction of aquaculture ponds based on Google Earth Engine. *Ocean Coast. Manag.* **2020**, *198*, 105348. [[CrossRef](#)]
46. El Din, E.S. A novel approach for surface water quality modelling based on Landsat-8 tasselled cap transformation. *Int. J. Remote Sens.* **2020**, *41*, 7186–7201. [[CrossRef](#)]
47. Wu, Q.; Miao, S.; Huang, H.; Guo, M.; Zhang, L.; Yang, L.; Zhou, C. Quantitative Analysis on Coastline Changes of Yangtze River Delta Based on High Spatial Resolution Remote Sensing Images. *Remote Sens.* **2022**, *14*, 310. [[CrossRef](#)]
48. Yang, C.; Xia, R.; Li, Q.; Liu, H.; Shi, T.; Wu, G. Comparing hillside urbanizations of Beijing-Tianjin-Hebei, Yangtze River Delta and Guangdong–Hong Kong–Macau greater Bay area urban agglomerations in China. *Int. J. Appl. Earth Obs. Geoinf.* **2021**, *102*, 102460. [[CrossRef](#)]
49. Chen, C.; Liang, J.; Xie, F.; Hu, Z.; Sun, W.; Yang, G.; Yu, J.; Chen, L.; Wang, L.; Wang, L.; et al. Temporal and spatial variation of coastline using remote sensing images for Zhoushan archipelago, China. *Int. J. Appl. Earth Obs. Geoinf.* **2022**, *107*, 102711. [[CrossRef](#)]
50. Jia, M.; Wang, Z.; Mao, D.; Ren, C.; Wang, C.; Wang, Y. Rapid, robust, and automated mapping of tidal flats in China using time series Sentinel-2 images and Google Earth Engine. *Remote Sens. Environ.* **2021**, *255*, 112285. [[CrossRef](#)]
51. Yang, X.; Zhu, Z.; Qiu, S.; Kroeger, K.D.; Zhu, Z.; Covington, S. Detection and characterization of coastal tidal wetland change in the northeastern US using Landsat time series. *Remote Sens. Environ.* **2022**, *276*, 113047. [[CrossRef](#)]
52. Liu, K.; Su, H.; Li, X.; Wang, W.; Yang, L.; Liang, H. Quantifying spatial–temporal pattern of urban heat island in Beijing: An improved assessment using land surface temperature (LST) time series observations from LANDSAT, MODIS, and Chinese new satellite GaoFen-1. *IEEE J. Sel. Top. Appl. Earth Obs. Remote Sens.* **2016**, *9*, 2028–2042. [[CrossRef](#)]
53. Xu, L.; Wu, Z.; Zhang, Z.; Wang, X. Forest classification using synthetic GF-1/WFV time series and phenological parameters. *J. Appl. Remote Sens.* **2021**, *15*, 042413. [[CrossRef](#)]
54. Sun, Q.; Zhang, P.; Sun, D.; Liu, A.; Dai, J. Desert vegetation-habitat complexes mapping using Gaofen-1 WFV (wide field of view) time series images in Minqin County, China. *Int. J. Appl. Earth Obs. Geoinf.* **2018**, *73*, 522–534. [[CrossRef](#)]
55. Tian, L.; Wai, O.W.H.; Chen, X.; Li, W.; Li, J.; Li, W.; Zhang, H. Retrieval of total suspended matter concentration from Gaofen-1 Wide Field Imager (WFI) multispectral imagery with the assistance of Terra MODIS in turbid water–case in Deep Bay. *Int. J. Remote Sens.* **2016**, *37*, 3400–3413. [[CrossRef](#)]
56. Orimoloye, I.R.; Mazinyo, S.P.; Kalumba, A.M.; Nel, W.; Adigun, A.I.; Ololade, O.O. Wetland shift monitoring using remote sensing and GIS techniques: Landscape dynamics and its implications on Isimangaliso Wetland Park, South Africa. *Earth Sci. Inform.* **2019**, *12*, 553–563. [[CrossRef](#)]
57. Zhu, S.; Wan, W.; Xie, H.; Liu, B.; Li, H.; Hong, Y. An Efficient and Effective Approach for Georeferencing AVHRR and GaoFen-1 Imageries Using Inland Water Bodies. *IEEE J. Sel. Top. Appl. Earth Obs. Remote Sens.* **2018**, *11*, 2491–2500. [[CrossRef](#)]
58. Liu, Q.; Liu, G.; Huang, C.; Xie, C. Comparison of tasselled cap transformations based on the selective bands of Landsat 8 OLI TOA reflectance images. *Int. J. Remote Sens.* **2015**, *36*, 417–441. [[CrossRef](#)]
59. Yang, F.; Fan, M.; Tao, J. An Improved Method for Retrieving Aerosol Optical Depth Using Gaofen-1 WFV Camera Data. *Remote Sens.* **2021**, *13*, 280. [[CrossRef](#)]

60. Cheng, W.-C.; Chang, J.-C.; Chang, C.-P.; Su, Y.; Tu, T.-M. A Fixed-Threshold Approach to Generate High-Resolution Vegetation Maps for IKONOS Imagery. *Sensors* **2008**, *8*, 4308–4317. [[CrossRef](#)]
61. Lee, S.; Jin, C.; Choi, C.; Lim, H.; Kim, Y.; Kim, J. Absolute radiometric calibration of the KOMPSAT-2 multispectral camera using a reflectance-based method and empirical comparison with IKONOS and QuickBird images. *J. Appl. Remote Sens.* **2012**, *6*, 063594. [[CrossRef](#)]
62. Kauth, R.J.; Thomas, G.S. The tasseled cap—A graphic description of the spectral-temporal development of agricultural crops as seen by Landsat. In *LARS Symposia, Proceedings of the Symposium on Machine Processing of Remotely Sensed Data, West Lafayette, IN, USA, 29 June–1 July 1976*; The Institute of Electrical and Electronics Engineers, Inc.: New York, NY, USA, 1976; p. 159.
63. Crist, E.P.; Kauth, R.J. The tasseled cap de-mystified. *Photogramm. Eng. Remote Sens.* **1986**, *52*, 81–86.
64. Crist, E.P. A TM Tasseled Cap equivalent transformation for reflectance factor data. *Remote Sens. Environ.* **1985**, *17*, 301–306. [[CrossRef](#)]
65. Sheng, L.; Huang, J.-F.; Tang, X.-L. A tasseled cap transformation for CBERS-02B CCD data. *J. Zhejiang Univ. Sci. B* **2011**, *12*, 780–786. [[CrossRef](#)]
66. Chen, C.; Fu, J.; Zhang, S.; Zhao, X. Coastline information extraction based on the tasseled cap transformation of Landsat-8 OLI images. *Estuarine, Coast. Shelf Sci.* **2019**, *217*, 281–291. [[CrossRef](#)]
67. Tatsumi, K.; Yamashiki, Y.; Morante, A.K.M.; Fernández, L.R.; Nalvarte, R.A. Pixel-based crop classification in Peru from Landsat 7 ETM+ images using a Random Forest model. *J. Agric. Meteorol.* **2016**, *72*, 1–11. [[CrossRef](#)]
68. Gilbertson, J.K.; van Niekerk, A. Value of dimensionality reduction for crop differentiation with multi-temporal imagery and machine learning. *Comput. Electron. Agric.* **2017**, *142*, 50–58. [[CrossRef](#)]
69. Song, C.; Ren, H.; Huang, C. Estimating soil salinity in the Yellow River Delta, Eastern China—An integrated approach using spectral and terrain indices with the generalized additive model. *Pedosphere* **2016**, *26*, 626–635. [[CrossRef](#)]
70. Hu, X.; Xu, H. A new remote sensing index for assessing the spatial heterogeneity in urban ecological quality: A case from Fuzhou City, China. *Ecol. Indic.* **2018**, *89*, 11–21. [[CrossRef](#)]
71. Rahman, S.; Mesev, V. Change Vector Analysis, Tasseled Cap, and NDVI-NDMI for Measuring Land Use/Cover Changes Caused by a Sudden Short-Term Severe Drought: 2011 Texas Event. *Remote Sens.* **2019**, *11*, 2217. [[CrossRef](#)]
72. Zanchetta, A.; Bitelli, G.; Karnieli, A. Monitoring desertification by remote sensing using the Tasseled Cap transform for long-term change detection. *Nat. Hazards* **2016**, *83*, 223–237. [[CrossRef](#)]
73. Santra, A.; Mitra, S.S. A Comparative Study of Tasseled Cap Transformation of DMC and ETM+ Images and their Application in Forest Classification. *J. Indian Soc. Remote Sens.* **2014**, *42*, 373–381. [[CrossRef](#)]
74. Ahmed, O.S.; Franklin, S.E.; Wulder, M.A. Interpretation of forest disturbance using a time series of Landsat imagery and canopy structure from airborne lidar. *Can. J. Remote Sens.* **2014**, *39*, 521–542. [[CrossRef](#)]
75. Frazier, R.J.; Coops, N.C.; Wulder, M.; Kennedy, R. Characterization of aboveground biomass in an unmanaged boreal forest using Landsat temporal segmentation metrics. *ISPRS J. Photogramm. Remote Sens.* **2014**, *92*, 137–146. [[CrossRef](#)]
76. Kazar, S.A.; Warner, T.A. Assessment of carbon storage and biomass on minelands reclaimed to grassland environments using Landsat spectral indices. *J. Appl. Remote Sens.* **2013**, *7*, 073583. [[CrossRef](#)]
77. Kakooei, M.; Baleghi, Y. A two-level fusion for building irregularity detection in post-disaster VHR oblique images. *Earth Sci. Inform.* **2020**, *13*, 459–477. [[CrossRef](#)]
78. Singh, H.; Garg, R.D.; Karnatak, H.C. Online image classification and analysis using OGC web processing service. *Earth Sci. Inform.* **2019**, *12*, 307–317. [[CrossRef](#)]
79. Kakooei, M.; Baleghi, Y. Shadow detection in very high resolution RGB images using a special thresholding on a new spectral-spatial index. *J. Appl. Remote Sens.* **2020**, *14*, 016503. [[CrossRef](#)]
80. Yue, H.; Li, Y.; Qian, J.; Liu, Y. A new accuracy evaluation method for water body extraction. *Int. J. Remote Sens.* **2020**, *41*, 7311–7342. [[CrossRef](#)]
81. Prošek, J.; Gdulová, K.; Barták, V.; Vojar, J.; Solský, M.; Rocchini, D.; Moudrý, V. Integration of hyperspectral and LiDAR data for mapping small water bodies. *Int. J. Appl. Earth Obs. Geoinf.* **2020**, *92*, 102181. [[CrossRef](#)]
82. Wang, L.; Chen, C.; Zhang, Z.; Gan, W.; Yu, J.; Chen, H. Approach for estimation of ecosystem services value using multitemporal remote sensing images. *J. Appl. Remote Sens.* **2021**, *16*, 012010. [[CrossRef](#)]
83. Li, Y.; Dang, B.; Zhang, Y.; Du, Z. Water body classification from high-resolution optical remote sensing imagery: Achievements and perspectives. *ISPRS J. Photogramm. Remote Sens.* **2022**, *187*, 306–327. [[CrossRef](#)]
84. Chen, C.; Fu, J.; Gai, Y.; Li, J.; Chen, L.; Mantravadi, V.S.; Tan, A. Damaged Bridges Over Water: Using High-Spatial-Resolution Remote-Sensing Images for Recognition, Detection, and Assessment. *IEEE Geosci. Remote Sens. Mag.* **2018**, *6*, 69–85. [[CrossRef](#)]
85. Bode, C.A.; Limm, M.P.; Power, M.E.; Finlay, J.C. Subcanopy Solar Radiation model: Predicting solar radiation across a heavily vegetated landscape using LiDAR and GIS solar radiation models. *Remote Sens. Environ.* **2014**, *154*, 387–397. [[CrossRef](#)]
86. Burrell, T.K.; O'Brien, J.M.; Graham, S.E.; Simon, K.S.; Harding, J.S.; McIntosh, A.R. Riparian shading mitigates stream eutrophication in agricultural catchments. *Freshw. Sci.* **2014**, *33*, 73–84. [[CrossRef](#)]
87. Kałuża, T.; Sojka, M.; Wróżyński, R.; Jaskuła, J.; Zaborowski, S.; Hämmerling, M. Modeling of river channel shading as a factor for changes in hydromorphological conditions of small lowland rivers. *Water* **2020**, *12*, 527. [[CrossRef](#)]